

Performance of Orthotropic Steel Plate under Combined Fire Load and Axial Compression

Xu Gong^{1,*} and Anil K. Agrawal²

Submitted: 30 August 2024 Accepted: 19 November 2024 Publication date: 10 January 2025

DOI: 10.70465/ber.v2i1.11

Abstract: The orthotropic steel plate systems have been used widely in decks of long-span bridges because of their large capacity and economic advantages. Early experimental and analytical research on orthotropic steel plate systems has mainly focused on their behaviors during ambient conditions. This paper presents a detailed investigation of the axial capacity of the orthotropic steel plates under fire using a sequential thermal stress analysis framework. Temperature-dependent stress-strain relationship and thermal properties of steel have been taken into consideration in the finite element modeling. Different models and parameters such as fire model, material model, geometric imperfection, residual stress, and rib wall thickness have been discussed, and their effects on the axial strength of the plate have been studied and compared. Simulation results indicate that fire has significant deteriorating effects on the plate's axial capacity. Conventional simple fire models, which assume uniform surface fire loads, do not represent real fire scenarios and tend to overestimate the axial capacity of the plate compared to realistic fire scenarios. Initial imperfection and residual stress in the orthotropic steel plate have negligible effects on the axial capacity of the orthotropic steel plate system under fire conditions. Increasing the rib wall thickness could improve the plate's fire resistance.

Author keywords: Orthotropic steel plate; Fire; Buckling; Axial Capacity

Introduction

Advantages of orthotropic steel plates, such as lightweight, large capacity, and ease of construction, contribute to their popularity in engineering applications. Generally, orthotropic steel plates are categorized by the shape of stiffeners as—open-rib system and closed-rib system. The closed rib system, made from trapezoidal, U shape or V shape ribs, is characterized by having a larger torsional strength and better force distribution ability than the open-rib system, made from flat, angle, or bulb ribs.¹

One important factor that needs to be considered in the design of orthotropic steel plates is their stability conditions, especially when they are under compressive loads. Like common thin-walled structures, buckling usually controls the load capacity, other than the yield strength of the material. If orthotropic steel plates are used in cable-stayed and self-anchored suspension bridges, special attention may be needed since the decks of these bridges are usually subjected to huge compressive forces caused by gravity and live

loads. According to the design manual for orthotropic deck bridges,¹ three limit states relevant to the stability condition should be evaluated: (1) Local buckling of the deck plate between ribs; (2) Local buckling of the rib wall; (3) Buckling of the orthotropic panel between floor beams.

Numerous analytical studies have been carried out in recent decades to evaluate the strength of the orthotropic plates. Niwa et al.² have reviewed existing analytical approaches for evaluating the compressive strength of stiffened plates. Four methods have been discussed, including the orthotropic plate approach, beam-column approach, discretization methods such as the finite strip method or finite element method, and nonlinear bifurcation method. However, due to the difficulty and slow progress in analytical methods, finite element analysis has gradually become a popular tool in modeling the behavior of the orthotropic plate under complicated boundaries. Grondin et al.³ have investigated the buckling behavior of steel plates stiffened with tee-shape stiffeners subjected to combinations of axial compression and bending using a finite element model. Different parameters, including initial imperfections in the plate, residual stress magnitude, plate slenderness ratio, plate aspect ratio, and plate-to-stiffener cross-sectional area ratio, were considered in the analysis. Their effects on the axial capacity and failure mode have also been discussed. Sheikh et al.⁴ analyzed the behavior of a continuously stiffened steel plate under combined uniaxial compression and bending moment using the finite element model developed by Grondin et al.⁵. Effects of parameters such as the transverse

*Corresponding Author: Xu Gong.

Email: gongxu291@hotmail.com

¹Adjunct professor, Department of Civil Engineering, Jingtangshan University, Ji'an City, Jiangxi Province, P.R.China

²Professor, Department of Civil Engineering, City College of New York, New York, NY, 10031

Discussion period open till six months from the publication date. Please submit separate discussion for each individual paper. This paper is a part of the Vol. 1 of the International Journal of Bridge Engineering, Management and Research (© BER), ISSN 3065-0569.

slenderness of the plate, the slenderness of the web and flange of the stiffener, and the ratio of areas of the stiffener to plate area on the response of the plate have been studied in detail. Shin et al.⁶ investigated the compressive capacity of the orthotropic plates stiffened with U-ribs based on finite element analysis and compared the numerical results with those of existing standards. This study shows that the results obtained from Eurocode 3 EN 1993-1-5 and FHWA-TS-80–205 are too conservative when column slenderness parameters are large. Zhang et al.⁷ employed an equivalent orthotropic material modeling (EOMM) method in which stiffeners are modeled as equivalent shell elements to study the static and dynamic response of a short-span bridge. The results were compared to those obtained from the original model with real geometry and materials. Gong and Agrawal⁸ used a nonlinear finite-element model to simulate different fire scenarios on a steel orthotropic box girder to investigate the stability of long-span cable-supported bridges. Li et al.⁹ conducted a parametric analysis based on FE models to investigate the buckling modes of the stiffened steel plates under axial compression. The sensitivity of the model to the residual stresses and initial imperfections was investigated. Other parameters, such as material properties and geometric dimensions, were also studied. Wang et al.¹⁰ simulated an orthotropic steel plate set with different U ribs and load conditions. The load-displacement curves were developed, and the bearing capacity of the plates set were compared.

In terms of experimental studies, Grondin et al.⁵ tested the capacity of steel plates stiffened with T-shaped stiffeners subjected to compression and bending. The residual stress and initial imperfection of the tested specimens were measured and employed in the numerical validation model. Chen and Yang¹¹ have examined the in-plane strength of an orthotropic deck system stiffened by U-shaped stiffeners. Test results have shown that local buckling failure may occur if current specifications are followed in the design. It is suggested that the width-to-thickness ratio of the deck plate and the U-shaped stiffeners should be limited in the design of an orthotropic deck system to avoid local buckling. Chou et al.¹² have conducted reduced-scale specimen tests of orthotropic plates with U- and T-shaped ribs. Results from experiment and finite element analysis have shown that the compressive strength obtained from finite element analysis agreed favorably with test results. Kumar et al.¹³ have studied experimentally and analytically the behavior of an orthogonal stiffened plate with flat bar stiffeners subjected to axial and lateral loads. It has been observed that the finite element analysis results matched with experimental data quite well. This study has also suggested that the inclusion of initial imperfection and residual stresses could produce an even better agreement between experimental and simulation results. Wang et al.¹⁰ tested three full-scale orthotropic steel plates set with single U-rib, double U-ribs and three U-ribs. The buckling mode, displacement, and strain distribution under various loading conditions were analyzed. He et al.¹⁴ carried out experimental studies with a series of orthotropic steel decks with open ribs subjected to axial compression loads to investigate the buckling behavior of the Zhang-Jing-Gao Yangtze River Bridge. Different factors, such as geometric

imperfections, residual stress, and live loads, have been tested to determine their influence on buckling behavior.

Currently, no analytical or experimental study results on the behavior of orthotropic steel plates during fire are available. Conventional simple fire models, which assume uniform surface fire loads, do not represent real fire scenarios and tend to overestimate the axial capacity of the plate compared to that during realistic fire scenarios. The main objective of this paper has been to investigate extensively the temperature-depending nonlinear behavior of the orthotropic plates using the finite element analysis approach consisting of nonlinear transient heat transfer analysis and nonlinear thermal-stress analysis approaches. In this approach, fire has been simulated by the Fire Dynamics Simulator (FDS), which can simulate a realistic fire curve (start phase, building up, and steady state). Different fire models, including simple fire models and computational fluid dynamics-based realistic fire models (e.g., FDS), have been created and compared. Sensitivity analysis of other modeling parameters, such as material models, initial geometric imperfection, residual stresses, and rib wall thickness, has also been carried out in the thermal-stress analysis. Their effects on the axial capacity of orthotropic steel plates during fire have been studied and compared. Simulation results show that the axial capacity predicted by the FDS fire model is the lowest among all fire models, even though the average temperature in the FDS fire is not the highest, i.e., simple fire models tend to overestimate the axial strength of the plate compared to the FDS fire model and should be used with caution. Compared to the simple fire models, the FDS model represents the real fire scenario better by considering the non-uniform spatial distribution of the fire load.

Structural Model

The prototype of the structural model is the orthotropic steel plate of the new San Francisco-Oakland Bay Bridge. A portion of its upper deck consisting of three U-ribs and a mid-floor beam tested by Chou et al.¹² is used in this numerical research. The top view of the deck is shown in Fig. 1. The finite element model of the orthotropic plate was created in ABAQUS¹⁵ and is shown in Fig. 2. Fig. 3 shows the cross-section A-A of the deck. The total number of nodes and elements in the finite element model are 23030 and 24588, respectively. In the heat transfer analysis, the 4-node quadrilateral shell element DS4 was used to model the deck plate and ribs, and the 3-node triangle element DS3 was assigned to the mid-floor beam and diaphragms at two ends. The boundary temperature history obtained from fire simulation was assigned to the corresponding surface node of the finite element model in ABAQUS. Nonlinear stress analysis has been conducted to investigate the behavior of the orthotropic steel plate under combined thermal and axial loads. A time-dependent temperature field obtained from the nonlinear transient heat transfer analysis step was applied to the model during the stress analysis. The stress/displacement fields of the structure were obtained, and behaviors of the orthotropic plate were assessed. The discretization of the

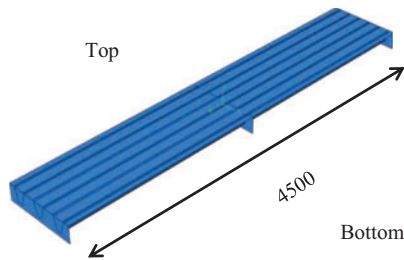


Figure 1. Prototype of the orthotropic plate (mm)

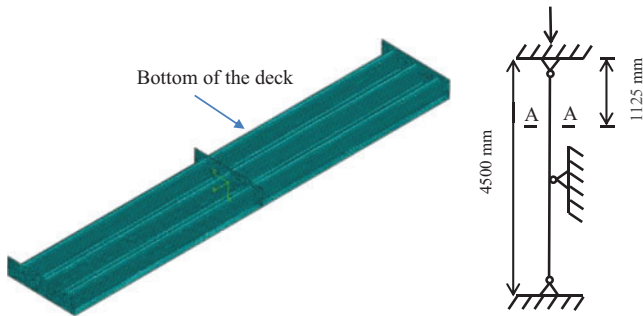
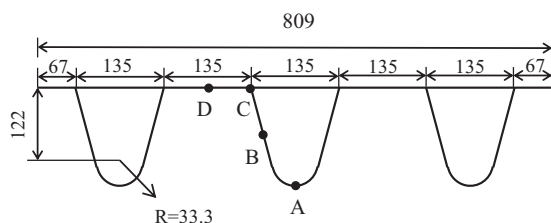


Figure 2. Finite element model and boundary condition



Thickness (mm): Deck plate=6mm; Rib plate=5mm
Steel type: ASTM A709 Grade 345 (345MPa)

Figure 3. Cross section A-A of the orthotropic plate

model was the same during heat transfer and nonlinear stress analyses. First-order shell elements S4R and S3 for stress/strain purposes were used accordingly for the plate and diaphragms. The maximum length of either of these elements was less than 12 mm and was decided by convergence analysis of stresses to an applied temperature field.

The plate was modeled to be simply supported at the top and bottom ends. An axial load along the longitudinal direction was applied in the displacement increment scheme. In particular, the mid-span floor beam was constrained in the lateral direction, as shown in Fig. 3. Diaphragms were installed at both ends to avoid local buckling. To improve model efficiency, boundary conditions and axial loads at both ends were prescribed to reference points, which are located at the geometric centers of two end sections.

The geometric imperfection in the steel members is usually caused by construction errors. The existence of geometric imperfection can significantly impair stability conditions and alter the buckling and post-buckling behavior of the loaded structural components. To reduce the negative effects of imperfection on the capacity of the compressive member, AASHTO¹⁶ imposes an upper limit

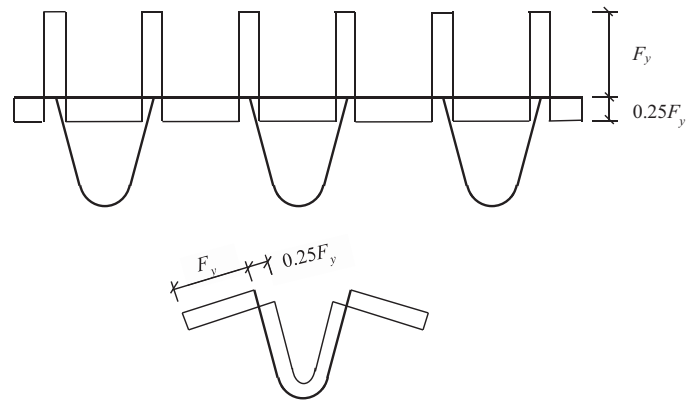


Figure 4. Distribution of residual stress in the orthotropic plate

for geometric imperfection as a fabrication requirement as $\frac{b}{26\sqrt{t_g}}$, where b is the width of the deck plate and t_g is the deck plate thickness.

In this study, the geometric imperfection in the 3D model was simulated by applying a uniform pressure in the normal direction of the deck plate. Then, the deflection pattern caused by pressure was tuned to match the measured error in the actual plate.¹²

Since limited data about the distribution of residual stress in orthotropic plates is available, the pattern defined by Fukumoto et al.¹⁷ and Grondin et al.¹⁸ has been adopted in this analysis. According to their studies, the magnitude of residual stress can be as large as the yielding stress of the steel at the connection area of the plate and ribs. The details of the residual stress distribution are shown in Fig. 4.

To study the effects of initial imperfection and residual stress on the axial capacity of the plate, three different cases were considered in the following stress analysis: (a) model with both imperfection and residual stress; (b) model with only the initial imperfection; and (c) ideal model without imperfection or residual stress.

The axial load-deformation curves obtained from the finite element model of the orthotropic steel plate during ambient conditions have been compared to those from experimental and numerical studies by Chou et al.¹² and the numerical study by Shin et al.,⁶ as shown in Fig. 5. The plots in this figure show that the proposed model produces a load-deformation curve that matches well with those from experimental results and other available numerical studies. The proposed model has also captured the peak axial capacity of the orthotropic plate during tests. Hence, the finite element model of the orthotropic plate can predict axial behavior under ambient conditions very well.

Temperature-Dependent Material Properties

As the temperature increases, the mechanical properties, such as stress-strain relationship and elastic modulus, and thermal properties, such as specific heat, conductivity, and expansion, are changed considerably. The variation

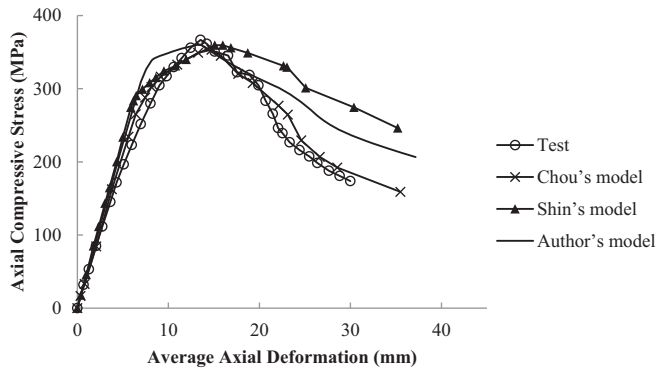


Figure 5. Axial load-deformation relationship under ambient temperature

of material properties significantly affects the structural behavior during the fire. This section briefly describes the temperature-dependent material models used in the analysis.

Temperature-dependent stress-strain relationship

Detailed information on the temperature-dependent stress-strain relationship of steel is presented in Eurocode-3,¹⁹ Poh,²⁰ and Lie.²¹ Temperature-dependent models described in Eurocode-3 (EC3) and Poh have been utilized and compared for the nonlinear stress analysis in this paper. High-temperature creep is considered implicitly by the EC3 model, but it is not included in Poh's model. Fig. 6 compares the stress-strain relationship for 345 MPa steel calculated by Poh's model and EC3 model at 20, 200, 500, 800 and 1000 °C temperatures. It is shown that both models produce matching curves at low and intermediate temperatures. When the temperature is high, the strength predicted by Eurocode-3 is more conservative than by Poh's Model.

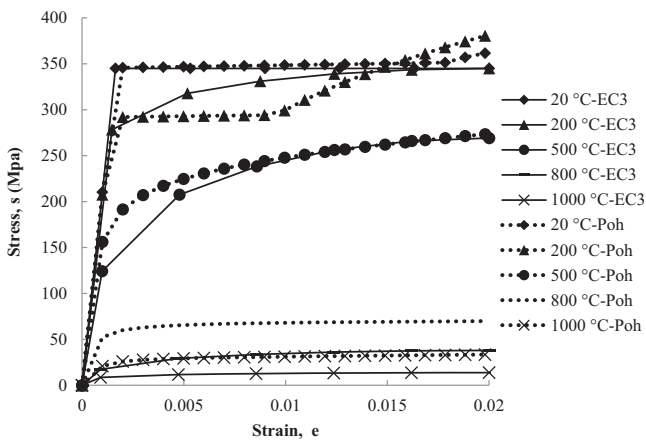


Figure 6. Temperature-dependent stress-strain relationship from the EC3 model and Poh's Model

Fire Model

Three different fire models, namely the standard fire model, hydrocarbon fire model, and Fire Dynamics Simulator (FDS) model, have been investigated. Both standard fire and hydrocarbon fire models, which assume a spatially uniform fire load over the structure, represent simple fire models. The FDS model, created based on computational fluid dynamics, is a more accurate representation of a real fire scenario.

Standard fire model

A fire load following the standard fire curve²² was applied to the bottom surface of the orthotropic plate through the convection heat transfer mechanisms. Here, the temperature-time relationship is given by:

$$T_{fi} = 345 \log(8t + 1) + T_a [^{\circ}\text{C}] \quad (1)$$

where T_{fi} is the gas temperature in the fire compartment; T_a is the ambient temperature, which is 20 °C in this paper; t is the exposure time in minutes. The convection heat transfer coefficient h is assumed to be 25 W/m²K in the thermal analysis. The resulting temperature history curve of the standard fire model is shown in Fig. 7.

Hydrocarbon fire model

Eurocode 1²² defines a more severe fire model caused by the burning of liquid fuel such as gasoline or petrol. The temperature curve for the hydrocarbon fire is defined by,

$$T_{fi} = 1080 \log(1 - 0.325e^{-0.167t} - 0.675e^{-2.5t}) + T_a [^{\circ}\text{C}] \quad (2)$$

where T_{fi} and T_a represent gas and ambient temperature, respectively. The coefficient of the convection, in this case, is assumed to be 50 W/m²K according to the standard. The temperature history for the hydrocarbon fire model and its comparison with the standard fire model are shown in Fig. 7. It is observed that the time-dependent temperature reached during a standard fire is significantly smaller than that during a hydrocarbon fire.

CFD fire model

Standard and hydrocarbon fire models have been used widely to evaluate the fire resistance of the structural

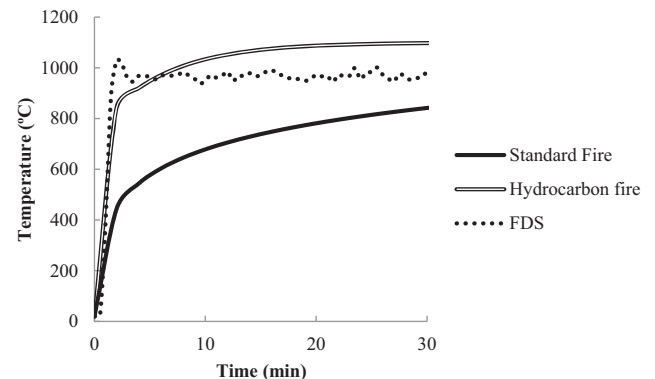


Figure 7. The gas temperature for fire models

members. The energy released during a fire is generally non-uniformly distributed. A more realistic fire modeling can be carried out using the computational fluid dynamics theory. Fire Dynamics Simulator (FDS) is a computer program that simulates the evolution of fire by solving the Navier-Stokes equations.²³ Unlike the simplified fire model, the FDS model can reproduce a relatively more realistic fire scenario by prescribing non-uniform heat flux over the exposure surface.²³

The front and bottom views of the geometric model of the orthotropic steel plate developed in FDS are shown in Fig. 8. The geometry of the plate is based on the upper deck of the new San Francisco-Oakland Bay Bridge, as shown in Fig. 2. In Fig. 8, the brown objects represent the deck plate and floor beam, and the grey color represents the ribs. The green dots are locations where temperatures have been recorded during the heating process. Since the geometry in FDS can only be constructed with rectangular obstructions, the U-shaped ribs of the orthotropic plate do not conform to the rectangular mesh. Instead, rectangular obstructions that approximate U-shaped ribs have been employed in the geometric model. The structural components were assumed to have the properties of steel (density of 7,850 kg/m³).

To create a fire model in FDS, a heat release rate per unit area (HRRPUA) vs. time relationship based on fuel properties needs to be defined. Karlsson and Quintiere²⁴ proposed a simple form of the HRRPUA curve that includes three stages of fire: growth phase, steady phase, and decay phase. The t-squared fire modeled by Eq. (3) with the growth rate (α) of 0.19 kW/s² [National Fire Protection Association (NFPA)²⁵] has been used to describe the growth phase.

$$\dot{Q} = \alpha t^2 \quad (3)$$

In Eq. (3), \dot{Q} is the heat release rate, α denotes a growth factor, and t is the time from established ignition in seconds.

A hypothetical fire with a maximum Heat Release Rate per Unit Area (HRRPUA) of 3290 kW/m²²⁶ was created in FDS. In most real situations, the fire department should reach the site within a very short time to secure the safety of people and properties. The first 30 minutes are therefore

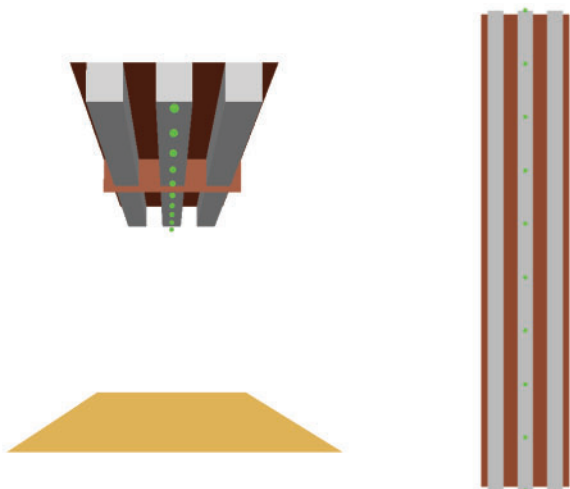


Figure 8. Geometric model in FDS

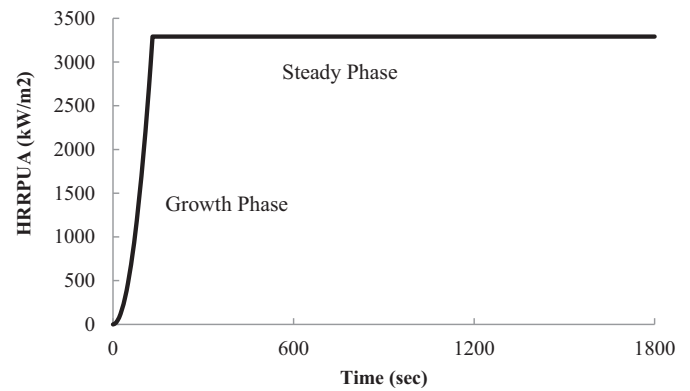


Figure 9. Designed fire curve used in FDS modeling

critical and is of our research interest in this paper. In this study, no decay phase was considered, and the steady phase was assumed to continue till the end of the simulation. The corresponding HRRPUA-Time relationship is shown in Fig. 9. It is observed that the fire reaches the steady state at $t = 132$ sec and continues to 1800 sec.

A domain of 1.2 m wide, 2.0 m deep, and 26.0 m high was created in FDS. The size of the domain was selected based on trial and error. The purpose is to allow for the sufficient development of flames while reducing the computation effort. All boundaries of the domain were assumed to be open to the exterior environment, and the initial temperature was 20°C.

The average air temperature history close to the bottom plate is shown in Fig. 7 using the FDS fire. This figure also shows comparisons with standard and hydrocarbon fires. It is observed from Fig. 7 that the air temperature obtained using the FDS fire model increases rapidly during the first 2 minutes and then fluctuates around 1000°C. The magnitude of the temperature is generally higher than that during the standard fire but is lower than that during the hydrocarbon fire.

Technical Approach

The concept of sequentially coupled thermal-stress analysis illustrated in the flowchart in Fig. 10 has been applied to investigate fire dependent behavior of orthotropic plates. In the first step, a fire model was created, and the corresponding firepower and duration were specified. For the simple fire model, it is defined by prescribed gas temperature-time history. Two types of simple fire models, the standard fire model and the hydrocarbon model, have been used for the research of orthotropic steel plates under fire loadings. For the realistic fire modeling, the geometric model of the structure was first built in a separate fire modeling program, namely Fire Dynamic Simulator (FDS), based on available drawings. The simulation results from FDS provided spatial-temporal temperature distribution over the structural boundary surfaces, which were applied in the second step.

In the second step, the internal temperature distribution of the structural model is obtained through the heat transfer analysis. A 3D finite element model of the orthotropic steel

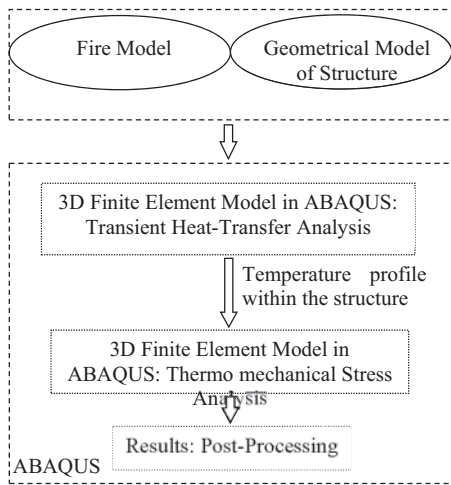


Figure 10. Framework of sequentially coupled thermal-stress analysis

plate was established in ABAQUS to carry out thermal analysis. For the realistic fire, the surface temperature distribution obtained from FDS was applied to the finite element model. Then, the temperature profile within the structure was computed through nonlinear heat conduction analysis.

The last step of this approach is the nonlinear 3D structural analysis with the consideration of temperature effects. The time-dependent temperature profile within the structural member was included in the stress analysis as

a predefined field. Temperature-dependent thermal and mechanical properties of the material were considered in the material model. Finally, the stress/strain field of the structure was obtained through the nonlinear static analysis.

Results and Discussion

Extensive simulation investigations carried out on orthotropic plates include (i) non-linear transient heat transfer analysis for predicting the temperature response using different fire models; (ii) non-linear stress analysis for computing the capacity under combined fire load and axial load; (iii) sensitivity study of modeling parameters.

To investigate the effect of modeling parameters on the axial capacity of orthotropic steel plates under combined fire and compressive loads, a group of models with different combinations of parameters has been created for comparison. The details of the simulation cases are summarized in Table 1.

Heat transfer analysis

Prior to stress analysis, the thermal response of the orthotropic steel plate to fire was simulated based on heat transfer analysis by imposing a specific set of initial boundary conditions. Temperature-dependent thermal properties of steel, such as thermal conductivity and specific heat

Table 1. Analytic model details

Model name	Material model	Fire load	Initial imperfection	Residual stress	Rib thickness (mm)
EC3-A-I-R	Eurocode-3	Ambient	Yes	Yes	5
EC3-S-I-R	Eurocode-3	Standard fire	Yes	Yes	5
EC3-S-I	Eurocode-3	Standard fire	Yes	No	5
EC3-S	Eurocode-3	Standard fire	No	No	5
EC3-H-I-R	Eurocode-3	Hydrocarbon fire	Yes	Yes	5
EC3-H-I	Eurocode-3	Hydrocarbon fire	Yes	No	5
EC3-H	Eurocode-3	Hydrocarbon fire	No	No	5
EC3-F-I-R	Eurocode-3	FDS fire	Yes	Yes	5
EC3-F-I-R-25%	Eurocode-3	FDS fire	Yes	25%	5
EC3-F-I-R-50%	Eurocode-3	FDS fire	Yes	50%	5
EC3-F-I-R-75%	Eurocode-3	FDS fire	Yes	75%	5
EC3-F-I	Eurocode-3	FDS fire	Yes	No	5
EC3-F	Eurocode-3	FDS fire	No	No	5
EC3-F-I-R-3	Eurocode-3	FDS fire	Yes	Yes	3
EC3-F-I-R-4	Eurocode-3	FDS fire	Yes	Yes	4
EC3-F-I-R-5	Eurocode-3	FDS fire	Yes	Yes	5
EC3-F-I-R-6	Eurocode-3	FDS fire	Yes	Yes	6
Poh-A-I-R	Poh's	Ambient	Yes	Yes	5
Poh-S-I-R	Poh's	Standard fire	Yes	Yes	5
Poh-H-I-R	Poh's	Hydrocarbon fire	Yes	Yes	5
Poh-F-I-R	Poh's	FDS fire	Yes	Yes	5

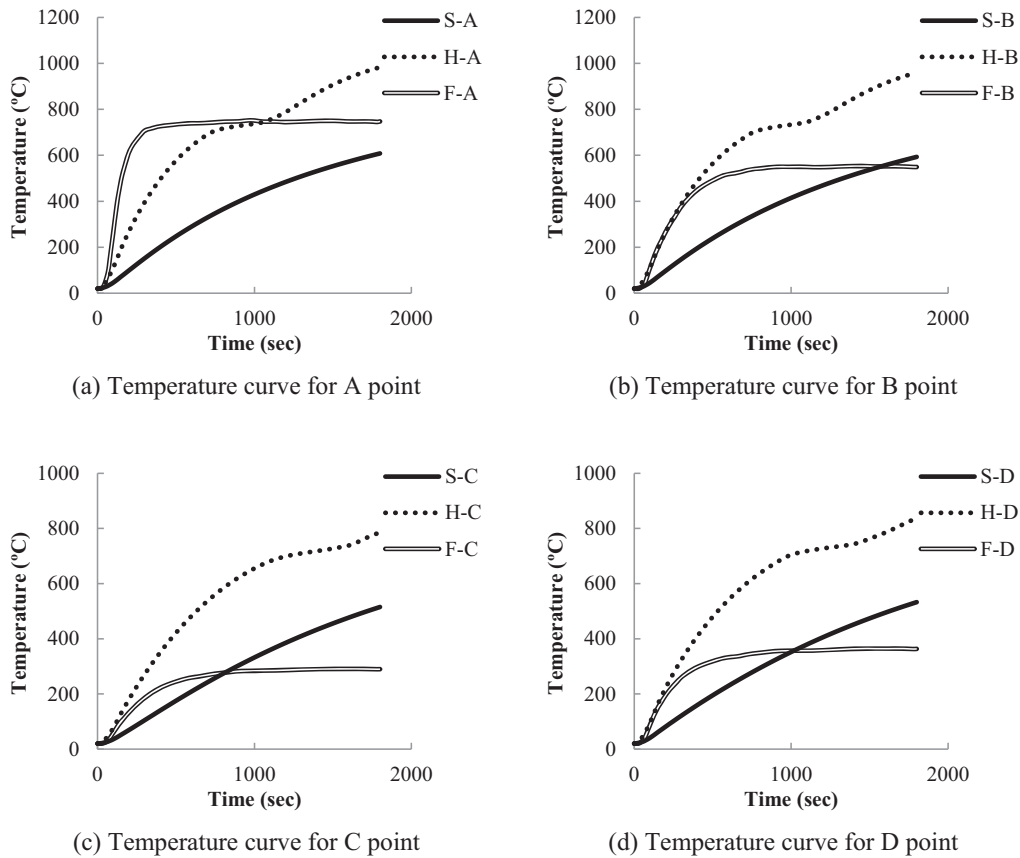


Figure 11. Temperature histories at points A, B, C, and D on the cross-section A-A. Note: S represents standard fire; H represents hydrocarbon fire; F represents FDS fire.

defined in Eurocode-3,²⁷ were included for the entire plate model.

Standard fire

A standard fire model was created, and the corresponding fire load was applied to the bottom side of the orthotropic steel plate. The initial temperature was set to be 20°C for the whole structure. Fig. 11 shows the temperature histories at points A, B, C, and D on the cross-section A-A of the plate in Fig. 2 when subjected to standard fire. The location of cross-section A-A is shown in Fig. 3. The temperature time histories in Fig. 11 show an upward trend for these monitored points. It is also observed that the temperature at the plate (points C and D) is generally lower than that at the ribs (points A and B). It implies that a nonlinear temperature gradient developed through the depth of the plate cross-section because the bottom surface of the plate was directly exposed to the fire load.

The temperature distribution of the rib and deck plate at 100 s, 300 s, 600 s, and 1800 s after the start of the fire are shown in Fig. 12. It is shown that the temperature profile at different cross sections was the same along the longitudinal direction of the plate as the standard fire model assumes a uniformly distributed heat convection. There are some variations of temperature field at areas near the two diaphragms and mid-floor beam because of the change of

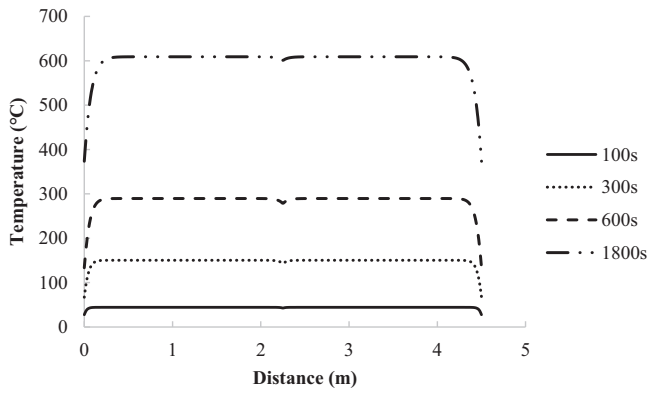
geometry. It can be observed that the temperature of the rib is almost 100°C higher than the deck plate.

Hydrocarbon fire

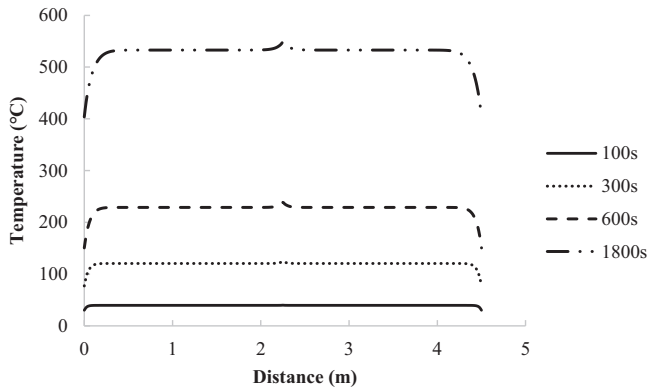
Fig. 11 shows the temperature histories at points A, B, C, and D under hydrocarbon fire. It is observed that the temperature increases rapidly with the development of the fire. Since the convection and air temperatures for the hydrocarbon fire model are larger than those for the standard fire model, the average temperature reached in the orthotropic plate was much higher. The temperature distribution of the rib and deck plate at 100 s, 300 s, 600 s, and 1800 s after the fire started is shown in Fig. 13. It is observed from Fig. 13 that the pattern of temperature distribution is similar to that during the standard fire case. The highest temperature also occurred at the rib with a magnitude of 985°C.

FDS fire

The surface temperature generated from FDS was specified as the boundary condition for the exposed surface in the finite element model. Temperature time histories at points A, B, C, and D for the FDS fire are shown in Fig. 11. It is observed that the temperatures at monitored points gradually stabilized after the growth phase. Fig. 14 shows the temperature distribution of the rib and deck plate at time instants of 100 s, 300 s, 600 s, and 1800 s after the fire started. Compared to the results during standard and hydrocarbon



(a) Rib



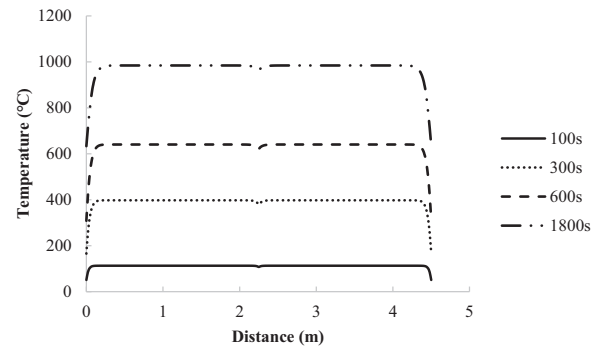
(b) Deck plate

Figure 12. Temperature distribution of rib and deck plate along the deck length under standard vfire

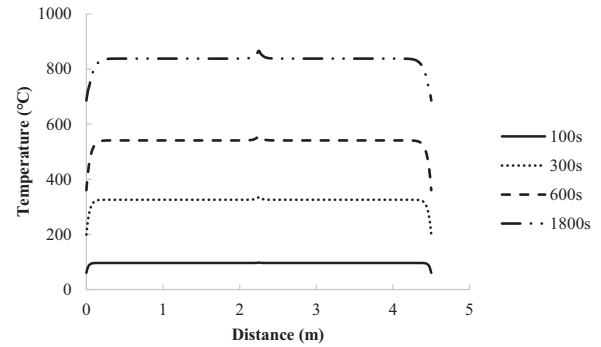
fire in Figs. 12 and 13, respectively, the temperature distribution obtained from FDS fire is less uniform, as shown in Fig. 14. It reflects the non-uniform heat flux generated by the fire and is a better representation of the real fire scenario.

Thermal-stress analysis

Based on the heat transfer analysis results, nonlinear stress analysis was performed to evaluate the axial capacity of the orthotropic plates under different fire conditions. A 3D thermo-mechanical finite element model has been created with four-node shell elements (S4R) for the plate and ribs and three-node shell elements (S3) for the end diaphragm and mid-floor beam. The result of heat transfer analysis provides the spatial-temporal temperature fields for all structural members of interest. The output of the thermal analysis is in the form of a time-temperature curve at every node in the thermal finite element model. The thermal models are then subjected to gravity loading and boundary conditions to perform structural analysis in a sequential manner. The temperature-dependent stress-strain relationship defined by Eurocode-3²⁷ and Poh²⁰ has been considered for a comparative study. Other modeling parameters, such as initial imperfection and residual stress, were considered for the sensitivity analysis. A total of 23 hypothetical cases have been simulated. The ultimate compressive strength of the plate F_u

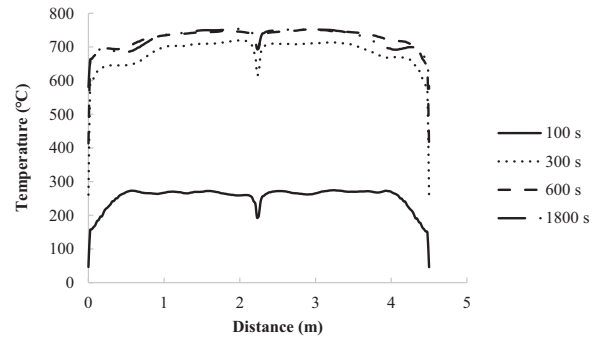


(a) Rib

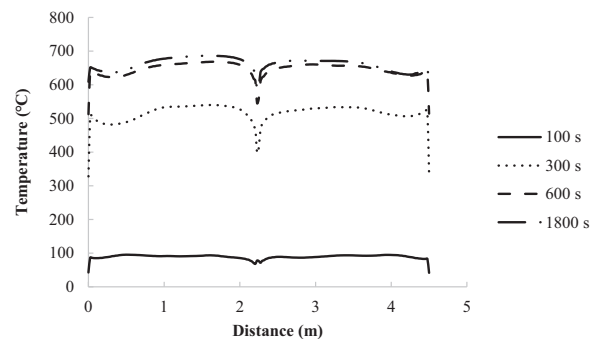


(b) Deck plate

Figure 13. Temperature distribution of rib and deck plate along the deck length under hydrocarbon fire



(a) Rib



(b) Deck plate

Figure 14. Temperature distribution of rib and deck plate along the deck length under FDS fire

and time to reach it t_u obtained for each case are summarized in Table 2.

Table 2. Ultimate strength (F_u) and Time to Reach Ultimate Strength (t_u)

Model name	t_u (sec)	F_u (MPa)	Difference of F_u compared to ambient test result (371 Mpa)
EC3-A-I-R	574.87	362.99	2.16%
EC3-S-I-R	317.85	347.24	6.40%
EC3-S-I	229.56	378.88	-2.12%
EC3-S	236.49	384.65	-3.68%
EC3-H -I-R	163.17	332.94	10.26%
EC3-H -I	141.90	345.09	6.98%
EC3-H	142.58	345.57	6.85%
EC3-F-I-R	117.56	305.58	17.63%
EC3-F-I-R-75%	138.16	329.57	11.17%
EC3-F-I-R-50%	125.69	328.06	11.57%
EC3-F-I-R-25%	138.16	327.77	11.65%
EC3-F-I	125.69	323.42	12.82%
EC3-F	112.43	318.88	14.05%
EC3-F-I-R-3	119.42	241.93	34.79%
EC3-F-I-R-4	122.69	302.33	18.51%
EC3-F-I-R-5	117.56	305.58	17.63%
EC3-F-I-R-6	126.79	311.50	16.04%
POH-A-I-R	528.60	366.84	1.12%
POH-S-I-R	310.44	336.21	9.38%
POH-H-I-R	167.85	321.71	13.28%
POH-F-I-R	183.36	291.36	21.47%

Effect of fire models

Fig. 15 compares the predicted loading curves of the orthotropic plate subjected to standard, hydrocarbon, and FDS fires. Experimental results obtained by Chou et al.¹² under ambient conditions have also been plotted in the same figure. In the simulation, temperature dependent stress-strain relationship defined by EC3 has been used as the material property. Both initial imperfection and residual stress have been included in the finite element model. Under fire conditions, it is observed from Fig. 15 that axial stress in the plate increases much faster, and peak axial stress capacity was less than that during the ambient condition. This is

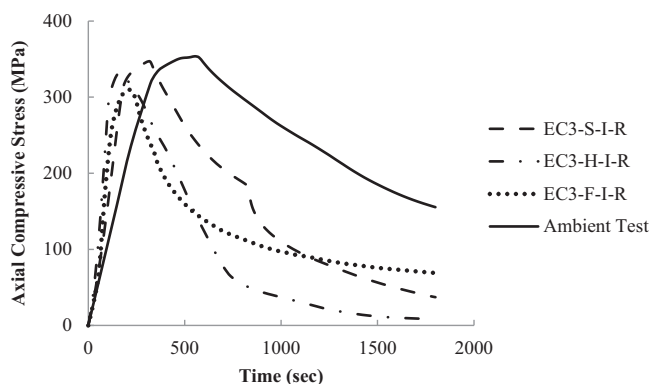


Figure 15. Load curves for different fire models

caused by the thermal expansion of the structural material. Significant stress was induced since the plate was restrained at both ends.

It is observed from Table 2 that the time to reach the ultimate strength (t_u) was decreased from 554 sec during the ambient condition to 317 sec for standard fire, 163 sec for hydrocarbon fire, and 118 sec for FDS fire. It is observed that the failure process was accelerated because of the effect of fire. The ultimate axial capacity of the plate (with respect to 371 MPa during ambient conditions) was reduced by 6.4%, 10.3%, and 17.6% during standard, hydrocarbon, and FDS fires, respectively. This shows that the fire has a significant deteriorating effect on the compressive capacity of orthotropic plates. The reduction in axial capacity can be attributed to the buckling caused by restrained thermal expansion.

Fig. 15 and Table 2 show that the reduction in the axial capacity under FDS fire is greater than under the other two fire models, although the average temperature reached during the FDS fire wasn't the highest. This is caused by the non-uniform distribution of the temperature fields and temperature gradient, which led to the uneven expansion of steel fibers. This caused displacement of the neutral axis, which resulted in extra moments acting on the plate. Surface temperature distributions during standard and hydrocarbon fires were relatively uniform in the longitudinal direction of the plate. In this sense, the FDS fire represented a better representation of a real fire. Overall, results using simple

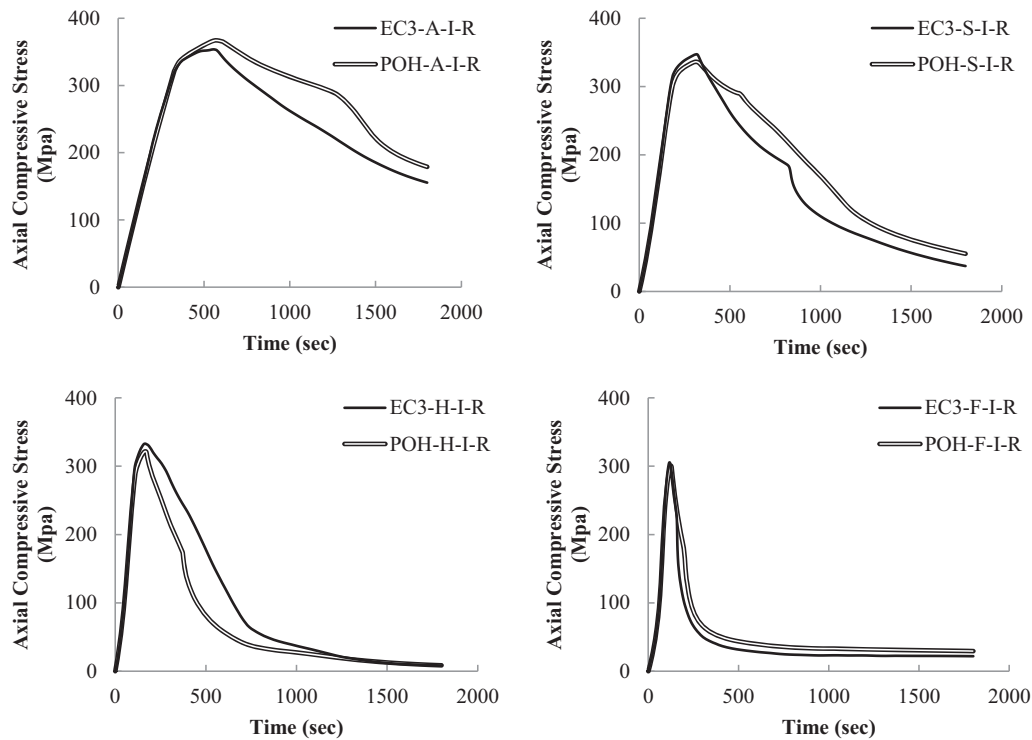


Figure 16. Load curves for EC3 and Poh's models

fire models tend to overestimate the axial force capacity of orthotropic plates.

Effect of material model

Two different temperature-dependent stress-strain relationships, namely the Eurocode-3 model and Poh's model, have been used in the nonlinear stress analysis. Both initial imperfections and residual stress have been considered in the finite element model. The loading curves obtained by using the Eurocode-3 model and Poh's model during ambient conditions, standard, hydrocarbon, and FDS fire models have been compared in Fig. 16.

It is observed from Fig. 16 that the ascending parts of the two curves agree very well, implying that both models captured the degradation of the stiffness at increasing temperatures. The axial capacity predicted by the EC3 model is slightly larger than that by Poh's model. The post-buckling behaviors, described by the descending part of the curves, using the two material models, also show good agreement. The simulation results show that both the EC3 model and Poh's model are reliable in predicting the axial behavior of the orthotropic steel plates under fire loads.

Effect of residual stresses

The residual stress distribution proposed by Fukumoto et al.¹⁷ and Grondin et al.¹⁸ has been applied to the finite element model. The temperature-dependent stress-strain relationship defined by the EC3 model has been used for temperature-dependent material behavior. Five independent cases with different residual stress distributions have been investigated under FDS fire. Specifically, the first scenario was assumed to have imperfections and zero residual stress

(FDS-S-I). The second to fifth scenarios were defined by 25% (FDS-S-I-R-25%), 50% (FDS-S-I-R-50%), 75% (FDS-S-I-R-75%), and 100% (FDS-S-I-R) of the residual stress, as considered in the study by Grondin et al.¹⁸.

Fig. 17 shows loading curves for orthotropic plates with different residual stresses under FDS fire. These plots show that increasing residual stress slightly reduced the axial capacity of the orthotropic plate. As shown in Table 2, residual stress reduced the axial capacity by approximately 8.4% under standard fire (EC3-S-I-R), 3.5% under hydrocarbon fire (EC3-H-I-R), and 5.5% under FDS fire (EC3-F-I-R) compared to cases without residual stresses (EC3-S-I, EC3-H-I, and EC3-F-I). It indicates that the effects of the residual stress can be neglected in the fire situation because of the decrease of the yield strength at high temperatures.

Effect of initial imperfection

Fig. 18 compares the loading curves for the plate models with and without imperfections. The EC3 model has been employed for the temperature-dependent material property in the finite element model. It is observed that the ascending portions of each pair of curves (with and without initial imperfection) are in good agreement with each other. However, the descending portions of these curves are seen to differ significantly from each other. In the plate with initial imperfection, the rate of decrease in axial stress is significantly slow. This shows that the post-buckling behavior of the orthotropic steel plates is significantly affected by initial imperfection.

Simulation results in Table 2 show that the initial imperfection had only a minor effect on the axial capacity of the orthotropic plate under different fire conditions. It is

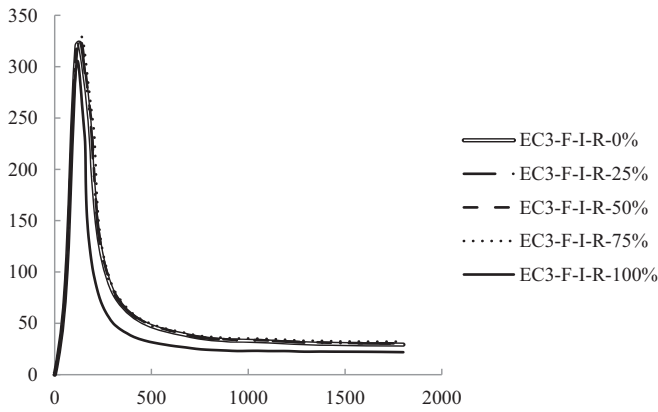


Figure 17. Loading curves for different residual stress levels

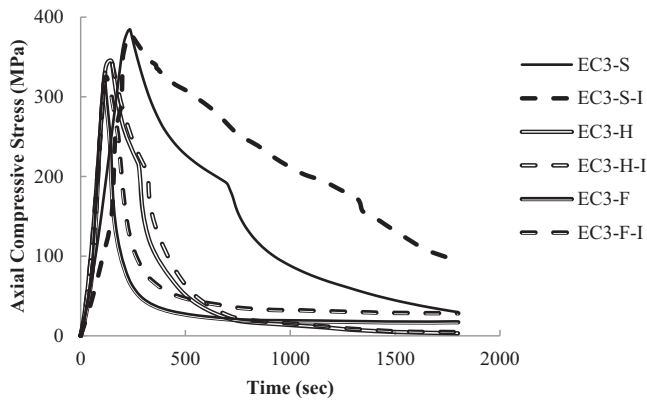


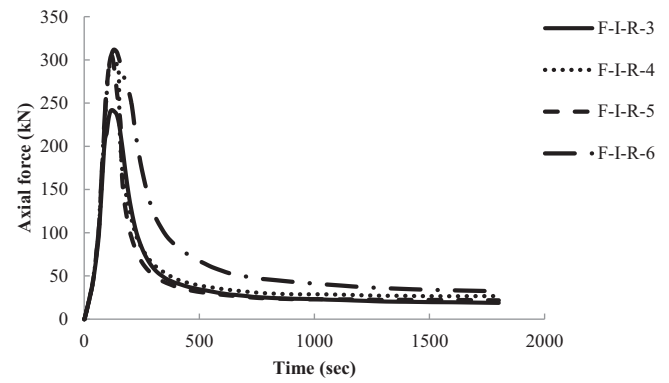
Figure 18. Loading curves for initial imperfection

observed that the axial capacity of the models without initial imperfection exceeded those with imperfections in less than 2% of all cases in Table 2. However, the time to reach the axial capacity has decreased considerably because of the existence of imperfection. For example, when the plate was subjected to FDS fire, the time to reach axial capacity (t_u) in the case of EC3-F-I was 11% less than that in the case of EC3-F.

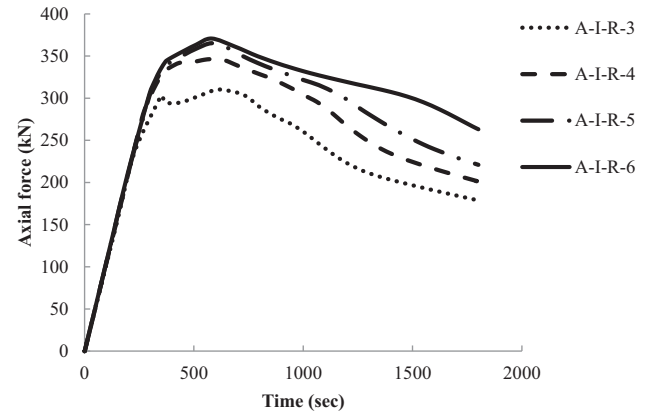
Effect of rib thickness

Fire resistance of orthotropic plates with different thicknesses of rib was compared under FDS fire. Six cases have been considered, each incorporating the EC3 material model, the same magnitude of initial imperfection and residual stress. Though rib wall thicknesses of 3 mm and 4 mm are impractical dimensions in actual design, these models were created to investigate the extreme conditions where elastic local buckling of the rib wall would control the mode of failure. Simulation results indicate that the rib wall buckled at the same location before yielding in 6 models, and failure modes were consistent.

Fig. 19 shows that the axial capacity of the orthotropic plate increased as the rib wall thickness got thicker. It is found that increasing the dimension of the rib wall is an efficient way to improve fire resistance. As shown in Fig. 19b and Table 2, the peak axial capacity of the orthotropic plate



(a) FDS fire



(b) Ambient condition

Figure 19. Loading curves for different rib thickness

under FDS fire was increased by 29% when rib wall thickness increased from 3 mm to 6 mm, compared to 22% under ambient conditions (Fig. 19a). Fig. 19b also shows that the axial capacity of the plate dropped rapidly after reaching the peak value. This indicates that the orthotropic plate failed within a very short time in fire.

Conclusion

This paper presents the state-of-the-art research on the behavior of the orthotropic steel plates during fire. The sequential thermal-stress analysis method has been employed to evaluate the axial capacity of orthotropic steel plates under different fire conditions. A series of cases have been simulated by varying modeling parameters, such as fire models, temperature-dependent stress-strain relationships, initial imperfection, and residual stress. Simulation results show that the axial capacity predicted by the FDS fire model is the lowest among standard, hydrocarbon, and FDS fire models, although the average temperature reached during the FDS fire is not the highest among the three fire models. Compared to the simple fire models, such as standard and hydrocarbon fire models, the FDS model represents the real fire scenario better by considering the non-uniform spatial distribution of the fire load. It is observed that simple fire models tend to overestimate the axial strength of the plate

compared to the FDS fire model and should be used with caution.

Among temperature-dependent fire models, both EC3 and Poh's models capture the critical behavior of the orthotropic plate with negligible differences. However, the axial capacity predicted by the EC3 model is slightly larger than that by Poh's model if other conditions are the same.

The effect of initial imperfection and residual stress on the plate's axial behavior under fire conditions resembled those under ambient conditions. They both deteriorated the capacity of the orthotropic plate. Simulation results show that certain level of residual stresses only has negligible effect on plate axial capacity under realistic fire.

Simulation results show that the axial capacity of the plate was improved by increasing the rib wall thickness of the plate. It provides evidence that increasing the member's dimension could be an effective way to promote the fire resistance of the orthotropic plate.

Experimental studies need to be carried out to evaluate the axial capacity of the orthotropic steel plate under fire. The simulation results presented herein can then be validated based on experimental observations.

References

- [1] Connor R, Fisher J, Gatti W, et al. *Manual for Design, Construction, and Maintenance of Orthotropic Steel Deck Bridges*. Washington, DC: FHWA; 2012.
- [2] Niwa Y, Watanabe E, Isami H. New approach to predict the strength of compressed steel stiffened plates. *Proceedings of the Japan Society of Civil Engineers*; Japan; 1985; pp. 35–44.
- [3] Grondin GY, Elwi AE, Cheng JJR. Buckling of stiffened steel plates—a parametric study. *J Constr Steel Res*. 1999;50(2):151–175. doi:10.1016/S0143-974X(98)00242-9.
- [4] Sheikh IA, Elwi AE, Grondin GY. Stiffened steel plates under combined compression and bending. *J Constr Steel Res*. 2003;59(7):911–930. doi:10.1016/S0143-974X(02)00079-2.
- [5] Grondin GY, Chen Q, Elwi AE, et al. Stiffened steel plates under compression and bending. *J Constr Steel Res*. 1998;45(2):125–148. doi:10.1016/S0143-974X(97)00058-8.
- [6] Shin DK, Le VA, Kim K. In-plane ultimate compressive strengths of HPS deck panel system stiffened with U-shaped ribs. *Thin-Walled Struct*. 2013;63(11):70–81. doi:10.1016/j.tws.2012.10.001.
- [7] Zhang W, Cai CS, Pan F. Finite element modeling of bridges with equivalent orthotropic material method for multi-scale dynamic loads. *Eng Struct*. 2013;54(7–8):82–93. doi:10.1016/j.engstruct.2013.03.047.
- [8] Gong X, Agrawal AK. Safety of cable-supported bridges during fire hazards. *J Bridge Eng*. 2016;21(4):04015082. doi:10.1061/(ASCE)BE.1943-5592.0000870.
- [9] Li Y, Liu Y, Liu R. Finite element analysis on axial compressive behaviors of high-performance steel stiffened plates in bridge application. *Int J Steel Struct*. 2019;19(5):1624–1644. doi:10.1007/s13296-019-00238-y.
- [10] Wang F, Tian LJ, Zhao Z, et al. Stability of full-scale orthotropic steel plates under axial and biased loading: experimental and numerical studies. *J Constr Steel Res*. 2021;181(122):106613. doi:10.1016/j.jcsr.2021.106613.
- [11] Chen SJ, Yang KC. Inelastic behavior of orthotropic steel deck stiffened by U-shaped stiffeners. *Thin-Walled Struct*. 2002;40(6):537–553. doi:10.1016/S0263-8231(02)00005-8.
- [12] Chou CC, Uang CM, Seible F. Experimental evaluation of compressive behavior of orthotropic steel plates for the new San Francisco-Oakland bay bridge. *J Bridge Eng*. 2006;11(2):140–150. doi:10.1061/(ASCE)1084-0702(2006)11:2(140).
- [13] Kumar MS, Kumar CL, Alagusundaramoorthy P, et al. Ultimate strength of orthogonal stiffened plates subjected to axial and lateral loads. *KSCE J Civil Eng*. 2010;14(2):197–206. doi:10.1007/s12205-010-0197-2.
- [14] He X, Wu C, Wang R, et al. Experimental study on buckling behavior of orthotropic steel deck with slender open ribs for large span suspension bridges. *J Constr Steel Res*. 2023;201:107681. doi:10.1016/j.jcsr.2022.107681.
- [15] Simulia. *Abaqus Analysis User's Manual, Version 6.11*. Providence, RI; 2011.
- [16] AASHTO. *Standard Specifications for Highway Bridges*. 17th ed. Washington, DC: American Association of State Highway and Transportation Officials, 2002.
- [17] Fukumoto Y, Usami T, Okamoto Y. Ultimate compressive strength of stiffened plates. *Proc., Specialty Conf. on Metal Bridge*; 1974; St. Louis, Mo.
- [18] Grondin GY, Wang E, Elwi AE. Interaction buckling of stiffened steel plates. *Proc., Structural Stability Research Council Annual Technical Session*; 2002; Washington, D.C: Structural Stability Research Council.
- [19] CEN (European Committee for Standardization), Actions on structures, Part 1.2. In: *Eurocode 1*. Brussels: CEN (European Committee for Standardization), 2000.
- [20] Poh KW. Stress-strain-temperature relationship for structural steel. *J Mater Civil Eng*. 2001;13(5):371–379. doi:10.1061/(ASCE)0899-1561(2001)13:5(371).
- [21] Lie TT (1992). *Structural fire protection: manual of practice*. In *ASCE Manual and Reports on Engineering Practice No. 78*. New York, NY: American Society of Civil Engineers.
- [22] CEN (European Committee for Standardization). Actions on Structures, Part 1.2. In: *Eurocode 1*. Brussels: CEN (European Committee for Standardization), 2002.
- [23] McGrattan K, McDermott R, Hostikka S, et al. *Fire Dynamics Simulator (Version 5): User's guide*. NIST, Gaithersburg, MD: Building Fire Research Laboratory, NIST; 2010.
- [24] Karlsson B, Quintiere J. *Enclosure Fire Dynamics*. Boca Raton, Florida: CRC press; 2002.
- [25] National Fire Protection Association (NFPA). *Guide for Smoke and Heat Venting*. Quincy, MA: NFPA 204M; 1985.
- [26] Nelson HE. *FPETOOL: Fire Protection Engineering Tools for Hazard Estimation*. Gaithersburg, MD: NISTIR 4380, National Institute of Standards and Technology; 1990.
- [27] Wang YC, Kodur VKR. Research toward use of unprotected steel structures. *J Struct Eng*. 2000;126(12):1442–1450.